Influence of ZnO nano-inclusions on the transport properties of the CoSb3 skutterudite

Caroline Chubilleau, Bertrand Lenoir, Philippe Masschelein, Anne Dauscher, Christophe Candolfi, E. Guilmeau, C. Godart

Influence of ZnO nano-inclusions on the transport properties of the skutterudite $CoSb_3$

C. Chubilleau[a,*], B. Lenoir[a], P. Masschelein[a], A. Dauscher[a], C. Candolfi[a], E. Guilmeau[b], C. Godart[c]

[a] *Université de Lorraine, CNRS, Institut Jean Lamour, Ecole Nationale Supérieure des Mines de Nancy, Parc de Saurupt, F-54042 Nancy, France*

[b] *CRISMAT-ENSICAEN, CNRS/UMR 6508, 6 Bd Maréchal Juin, 14050 Caen, France*

[c] *ICMPE-CMTR, CNRS-UMR 7182, 2-8 rue H. Dunant, F-94320 Thiais, France*

*Present address: CEA/LITEN/DTNM/LCSN, CEA Grenoble, 17 rue des Martyrs, F-38054 Grenoble cedex 09, France

Corresponding author: bertrand.lenoir@ijl.nancy-universite.fr, phone: +33 383 584 163, fax: +33 383 584 344

Addition of nanoparticles into bulk materials is one of the strategies designed to synthesize thermoelectric materials with superior efficiency. The presence of nanoparticles is expected to act as a barrier of the heat transport due to an increased amount of nanoscopic interfaces and to enhance the electronic properties via quantum confinement effects. Here, this approach was applied to the skutterudite $CoSb_3$ matrix in which different amounts of ZnO (2 – 12 wt%) nanoparticles were introduced. The samples were densified by spark plasma sintering and characterized by X-ray diffraction and scanning electron microscopy. The thermoelectric properties were investigated in a broad temperature range (2 – 800 K) to better assess the influence of the ZnO nanoparticles. The nanostructured materials showed a significant

enhancement in the thermopower values combined with a slight decrease in the thermal conductivity. A small amount of ZnO nanoparticles (2 wt%) has a beneficial influence on the dimensionless thermoelectric figure of merit *ZT* suggesting that introducing stable oxide nanoparticles may be an interesting way to improve the thermoelectric properties of skutterudite compounds.

Keywords: thermoelectric materials, composite materials, microstructure, thermoelectric properties

1. Introduction

The search for thermoelectric materials with higher efficiency is currently of prime interest in the field of renewable energy. Such materials can either convert waste heat (coming from sun, geothermal energy, cars or industrial processes…) to useable electricity, or can act as solid-state heat pumps when supplied with electrical current. The effectiveness of a material for thermoelectric applications is governed by the dimensionless figure of merit *ZT*, given by

$$ZT = \frac{S^2 T}{\rho(\kappa_e + \kappa_L)} \quad (1)$$

with T the absolute temperature and the following transport parameters: the Seebeck coefficient or thermopower S, the electrical resistivity ρ, the total thermal conductivity $\kappa = \kappa_e + \kappa_L$ where κ_e is the electronic thermal conductivity and κ_L is the lattice thermal conductivity [1]. Since S, ρ and κ_e are all sensitive to the carrier concentration, optimizing *ZT* is an extremely challenging task. Therefore, the *ZT* values of state-of-the-art thermoelectric materials based on $Bi_{1-x}Sb_x$, Bi_2Te_3, PbTe, and $Si_{1-x}Ge_x$ have been limited to unity for several decades [1-3].

Quite recently, skutterudite compounds have emerged as potential candidates for thermoelectric applications at high temperature [4]. The general chemical formula of binary skutterudites is MX_3, where M is a transition metal such as Co, Rh or Ir, and X stands for a pnictogen i.e. As, P or Sb. Some of them, such as $CoSb_3$, show good electrical properties (high carrier mobility and large effective mass) comparable to those of Bi_2Te_3 and PbTe. However, the large lattice contribution to the total thermal conductivity (~ 10 $W.m^{-1}.K^{-1}$ at 300 K for $CoSb_3$) is the main obstacle preventing to achieve high *ZT* values [5]. The presence of voids in the crystal structure of these compounds opened up a novel way to lower the

phononic part. Slack [6] suggested to fill these voids with weakly bound atoms that “rattle” about their equilibrium position. These voids can accommodate a large number of elements resulting in ternary derivatives $A_xM_4X_{12}$ referred as ‘filled skutterudites’ [7]. The presence of a filler atom in these cages induces an additional phonon scattering mechanism, usually modeled by an Einstein-like mode, which strongly dampens the lattice thermal conductivity [5,8]. This approach proved to be an efficient route to push the *ZT* values beyond unity [4,8-11].

Introducing nano-scaled structures into the bulk phase matrix is another approach for improving the thermoelectric properties that has received attention over the last years. Nanostructured materials have theoretically the potential to both enhance the electrical properties and limit the thermal conduction. The former feature is related to quantum confinement effects resulting in higher thermopower values [12]. The second property arises from the limitation of the phonon mean free path due to the presence of numerous nanoscopic interfaces. Several strategies have been developed to produce nanostructured $CoSb_3$ either by grain size reduction [13] or by dispersion of nanoparticles in the micrometric grained-sized matrix [14-16] or by creating in situ stable nanoinclusions [17]. Most of these last studies used mechanical mixing to introduce the nanoinclusions. These studies also mainly focused on filled skutterudites for which both the filler atoms and the nanoparticles modify the transport properties. The influence of the former thus obscures the role played by the latter preventing the underlying physical mechanisms to be investigated in detail. Such an approach was the starting point of the study of Su *et al*. [18].

Here, we report on the addition of ZnO nanoinclusions in the binary skutterudite $CoSb_3$ with the aim of determining the exact role played by stable oxide nanoparticles on the thermoelectric properties. The ZnO-$CoSb_3$ powders, fabricated using an ultrasonic mixing in liquid combined to freeze-drying, were densified by spark plasma sintering (SPS). Five

samples of $CoSb_3$ + x wt% ZnO were synthesized with x = 0, 2, 4, 8 and 12. The transport properties (including electrical, thermal and galvanomagnetic properties) of these specimens were investigated in a broad temperature range (2 – 800 K) and are discussed in light of the chemical and microstructural characterizations.

2. Experimental procedures

2.1. Materials synthesis

The preparation of the $CoSb_3$ + x wt% ZnO composites used in this study requires several steps. The first step is the synthesis of the $CoSb_3$ micron-sized particles starting from high purity Co powders (99.998%) and Sb shots (99.999). The metallurgical route utilized to prepare a $CoSb_3$ ingot is described in detail elsewhere [19]. The ingot was then crushed into μ-sized particles in an agate mortar. Nanosized ZnO powders were purchased from Alfa Aesar (APS powder, 99% with a measured size of about 100 nm). The micro and nano powders were mixed together during 20 min in a methanol/hexane (3:1) mixture at 0.025M in an ultrasonic bath respecting different weight ratio (x = 2% - 4% - 8% and 12%) of ZnO. The as-dispersed particles in the liquid were immediately immerged in liquid nitrogen and dried by freeze-drying during 12 hours (FTS-EZ585 system, 17 mTorr, -80°C). Finally, the composite powders were densified by SPS (Dr Sinter-515S) in graphite dies (10.4 mm in diameter) at 600°C during 6 min under 50 MPa. The densities of the obtained pellets were estimated from the mass and the geometry of the samples. The theoretical densities of the composites $d_{composite}$, reported in table I, were calculated using the formula

$$d_{composite} = \frac{1}{x/d_{ZnO} + (100 - x)/d_{CoSb_3}} \quad (2)$$

where d_{CoSb_3} and d_{ZnO} are the densities of $CoSb_3$ (7.64 g.cm^{-3}) and ZnO (5.67 g.cm^{-3}), respectively [20]. The relative densities (table I) decrease as the ZnO content in the $CoSb_3$

matrix becomes higher.

2.2. Chemical and structural characterizations and transport property measurements

The crystalline structures were investigated by X-ray diffraction (XRD) performed on a monochromatized CuKα_1 Bruker D8 Advance diffractometer equipped with a LynxEye detector. Information on the lattice unit cell was obtained via Rietveld refinement using the Fullprof software [21]. The micromorphology of the samples have been observed by scanning electron microscopy (FEG-SEM, Philips XL-30) in the secondary electron (SE) or back-scattered electron (BSE) mode on polished and fracture figures.

The SPS densified cylindrical samples were cut with a diamond wire saw into sub-parts for independent measurements of their physical properties. The measurement of the thermoelectric properties at low temperatures (2 – 300 K) were carried out using the thermal transport option (TTO) of the physical properties measurement system (PPMS, Quantum Design) on bar-shaped samples (typical dimensions 2.5×2.5×10 mm^3) which were cut perpendicularly to the pressing direction. The TTO allows sequential measurements of the electrical resistivity, Seebeck voltage and thermal conductivity at each temperature. For this measurement, four copper leads were attached onto the sample with conducting silver epoxy. Special care was taken to ensure good electrical and thermal contacts. A temperature gradient was established by applying heat at one end of the specimen while holding the other end at a constant temperature by maintaining good thermal contact with a low-temperature reservoir. Calibrated cernox thermometers were attached to the sample between 4 and 5 mm apart. The temperature difference was monitored and the voltage measured at the same positions along the sample. The data collected were corrected for thermal radiation by a modified model implemented in the TTO option software (from version 1.1.4) by Quantum Design. This model differs from that used in our prior work primarily in that it uses a more accurate

estimate of the bath temperature around the sample. The modified model results in a higher correction near 300 K thereby explaining the difference observed between our previous and present data sets [22]. Hall coefficient measurements were conducted between 5 – 300 K, on the same samples used for TTO measurements, using a five-probe method with the AC transport measurement system option of the PPMS. The electrical contacts were attached onto the samples with silver paste. The magnetic field was varied between ± 5 T to eliminate voltage probe misalignment effects.

For measurements over the 300 – 800 K temperature range, the thermopower and the electrical resistivity were simultaneously measured in a ZEM3-ULVAC device under partial helium atmosphere on bar-shaped samples. Thermal conductivity values were obtained from measurements of thermal diffusivity (NETZSCH, LFA 427) and specific heat (NETZSCH, DSC 403 F3) both realized under argon atmosphere. For the thermal diffusivity measurement, separate disks were sectioned from the same individual ingots.

Uncertainties in the electrical resistivity, Hall effect, thermopower and thermal conductivity measurements are at most 5%, 5%, 5% and 8 %, respectively. The results of the low and high temperature measurements match well near room temperature.

3. Results and discussion

3.1. Phase and microstructures

Figure 1 shows the XRD patterns of the $CoSb_3$ + x wt% ZnO after SPS. It can be seen that the matrix (x = 0) is a single-phase material with a minute amount of Sb as a secondary phase. The diffraction pattern is marked by distinct and narrow diffraction peaks. With the introduction of ZnO, new diffraction peaks appear whose intensities become higher with increasing the ZnO amount; those peaks correspond to the ZnO phase. Even for the lowest

ZnO content (2 wt%) added, peaks from the ZnO phase can be observed suggesting that ZnO is not finely dispersed in the $CoSb_3$ matrix. The lattice parameter (see table I) has been inferred from Rietveld refinement and was found constant regardless of the ZnO content.

The SEM analysis indicates that the $CoSb_3$ matrix is constituted of particles whose size is about 2-5 μm, as it can seen for example for the 2%ZnO-$CoSb_3$ sample (Fig. 2). This size is neither influenced by the presence of ZnO nor by its content. In addition, large ZnO aggregates are clearly observed at the grain boundaries of the composites, even for low percentages, but isolated aggregates are also present (Fig. 3). The areas where ZnO aggregates can extend up to hundreds of microns as the nominal percentage of ZnO is increased. These irregular micron-clusters have already been observed [14,23-25] in different composites with $CoSb_3$ as the matrix. The average size of the ZnO nanoparticles does not evolve with the SPS treatment and remains of the order of 100 nm. They present a pulverulent aspect (Fig. 2). This can be explained by the low sintering temperature used for skutterudites, too low to sinter ZnO whose sintering temperature is around 1200°C. This aspect likely induces higher porosity that explains the decreasing densities of the samples with the ZnO content (Fig. 3, table I).

3.2. Low-temperature thermoelectric properties

The temperature dependence of the thermopower for all the samples studied is shown in Figure 4. *S* is positive in the binary compound and in the composites suggesting that the holes are the dominant carriers. The positive sign of the Hall coefficient R_H further confirms this hypothesis (not shown here). Regardless of the composition, *S* rises monotonically with the temperature. Across the entire temperature range, the presence of ZnO inclusions induces

an increase of the *S* values. At 300 K, *S* ranges between 190 and 200 μV/K for *x* = 2, 4 and 8 wt% ZnO. Further increasing *x* to 12 wt% then lowers *S* that only reaches 165 μV/K.

The Hall coefficient R_H was found to be positive for all samples in agreement with the *S(T)* data. The hole concentration *p* was calculated from the values of R_H using the single-carrier formula $p = r_H / R_H e = 1 / R_H e$ (*e* is the elementary charge), whereby the Hall factor r_H was assumed to be equal to 1. *p* is displayed as a function of temperature in Figure 5 and the room temperature values are listed in table II.

As a first approximation, *p* can be considered as constant in the temperature range studied whatever the sample is. Surprisingly, these measurements revealed a decrease of *p* when the ZnO content increases. It is worth mentioning that ZnO is extremely stable and decomposes into zinc and oxygen only at 2348 K [26]. A decomposition of the ZnO nanoparticles during the SPS treatment therefore appears highly unlikely. Further, there is no report in the literature indicating that either Zn or O can substitute for Co or Sb or fill the structural voids. As a consequence, the decrease in the hole concentration with *x* suggests that holes could be trapped at the grain boundaries where ZnO and/or pores are present. It is known that most ZnO has *n*-type character due to unintentional incorporation of impurities acting as shallow donors [27]. It is thus probable that holes coming from the surface of the $CoSb_3$ grains diffuse into the ZnO barriers to form electron-hole pairs thereby reducing the itinerant carrier density.

The electrical resistivity as a function of temperature is shown in Figure 6 for the $CoSb_3$/ZnO composites. ρ shows a semiconducting behavior over the 2 – 300 K temperature range for all samples. The ρ values of pure $CoSb_3$ match those reported previously at comparable hole concentrations [28]. It appears that ρ increases with the addition of ZnO. At 300 K, the values are 1.5 to 12 times higher than that of the reference sample. At low temperatures however, the difference is more pronounced and reaches 3 orders of magnitude

at 2 K for the x = 12 wt% sample. As shown below, these results are consistent with mobility data indicating that the hole mobility is strongly degraded at low temperature when the concentration of ZnO increases.

Figure 7 shows the temperature dependence of the Hall mobility $\mu_H = R_H / \rho$ for all specimens. For $CoSb_3$ and the composites, μ_H increases with increasing temperature up to 300 K. In polycrystalline *p*-type $CoSb_3$ with comparable grain size, a $T^{3/2}$ variation standing for ionized impurity scattering, is usually the dominant scattering mechanism below 300 K [29]. Yet, this law cannot describe satisfactorily our experimental data. A better agreement can be obtained by fitting the $\mu_H(T)$ data with the equation

$$\mu_H = \frac{eL}{\sqrt{2\pi k_B T m^*}} \exp\left(-\frac{E_B}{k_B T}\right) \tag{3}$$

where L is the grain size, e is the elementary charge, m^* is the effective mass, k_B is the Boltzmann constant and E_B is the height of the energy barrier in the depletion region. This temperature dependence suggests that the grain boundaries dominate the hole diffusion as expected in samples with fine microstructure [30]. As can be seen in Figure 8, which depicts $\ln(\mu_H T^{1/2})$ vs $1/k_B T$, a nearly linear region appears between 150 and 300 K. Fitting this temperature range using Eq.(3) yields an activation energy E_B = 15 meV. When the average energy of the holes becomes higher than this energy barrier, the conduction is then dominated by thermionic emission (ballistic transport) following a $T^{-1/2}\exp(-E_B / k_B T)$ law. This mechanism dominates in this temperature range while at lower temperatures transport is dominated by thermally-assisted tunneling effects.

The $\mu_H(T)$ data of the composites show a steeper rise in temperature than that of the reference sample. However, the presence of ZnO is detrimental to the mobility of holes,

which drastically decreases. The impact of ZnO is more perceptible at low temperatures and all the more pronounced that the ZnO content is high. As for the scattering mechanisms, grain-boundary scattering seems to still play a role in the composites (cf. Fig. 7). This observation seems reasonable since the depletion layers formed at the ZnO/$CoSb_3$ interfaces are expected to behave as energy barriers impeding the conduction of holes between grains. The values of E_B deduced from the fit (see table II) are in line with those found in prior studies [31] and increases with the ZnO content suggesting that tunneling conduction decreases.

At equilibrium, the barrier height E_B and its width b are linked to the density of trapping states N_t and the carrier concentration p by [32]

$$E_B = \frac{e^2 N_t^2}{8\varepsilon_0 \varepsilon p} \tag{4}$$

$$b = \frac{1}{2}\frac{N_t}{p} \tag{5}$$

where ε_0 and ε are the permittivity of vacuum and of $CoSb_3$, respectively. The latter amounts to ε = 42.4 [33]. Table 2 summarizes the values of N_t and b for all the specimens. The density of trapping states seems independent of the ZnO concentration while the width increases with increasing x. Assuming $m^* = 0.07m_0$ (m_0 is the bare electron mass) [28,34,35], we estimated the effective grain size using Eq. (3) (Table II). The obtained values are consistent with the SEM images (cf. Fig. 2).

The low-temperature thermal conductivity data are plotted in Figure 9. At room temperature, a reduction close to a factor two can be observed for the 12 wt% ZnO composite. As mentioned above, the electrical resistivity of the ZnO/$CoSb_3$ composites is greater than 4 mΩ.cm for all x contents. These large values lead to an electronic thermal conductivity, κ_e, estimated using the Wiedemann-Franz law $\kappa_e = LT/\rho$ (L is the Lorenz number and equals

to 2.44×10^{-8} $V^2.K^{-2}$ for degenerate electron gas) which never exceeds 2% of the total thermal conductivity κ. Hence, the $\kappa(T)$ data almost entirely reflect the lattice thermal conductivity κ_L. The addition of ZnO into $CoSb_3$ does not influence the temperature dependence that remains typical of a dielectric crystal but decreases the values of κ_L. For x = 2, 4 and 8 wt% ZnO, this reduction is low but becomes more significant for x = 12 wt%. The decrease of the lattice thermal conductivity in the composite samples may be not only attributed to the large oxide defects localized at the grain boundaries but also to the porosity. However, a quantitative description of the role played by each of these mechanisms was not carried out in the present study but might be an interesting undertaking in future studies.

Figure 10 displays the calculated dimensionless figure of merit *ZT* versus *T*. For all samples, *ZT* increases with temperature. A significant enhancement of the *ZT* values by 30% at 300 K can be observed for the x = 2 wt% sample. Higher ZnO concentrations efficiently reduce the thermal conductivity but at the expense of a significant increase in the electrical resistivity. Thus, this combination leads to lower *ZT* values than those of the binary $CoSb_3$ compound in the whole temperature range.

3.3. High-temperature thermoelectric properties

The temperature dependences of the thermoelectric power of the binary $CoSb_3$ skutterudite and the ZnO/$CoSb_3$ composites are depicted in Figure 11. The four composites exhibit similar behaviours and values above 500 K. While this fact holds true for the x = 2, 4 and 8 wt% samples below this temperature, a sizable difference appears with the x = 12 wt% sample for which lower values are achieved. When the temperature rises, the *S* values peak before starting to decrease. The temperature at which the maximum occurs is near 520 K in $CoSb_3$ (S_{max} = 200 $\mu V.K^{-1}$) and is shifted to a lower temperature (450 K) when ZnO is added

(S_{max} = 252 μV.K^{-1}). No influence of the ZnO content on the temperature of this maximum is observed in the present data. Above 600 K, it can be noted that all materials of this series possess similar Seebeck coefficient values. The downturn observed is likely the signature of minority carrier effects. All samples enter the intrinsic domain of conduction.

The temperature dependence of the electrical resistivity is reported in Figure 12. As already highlighted by the low-temperature data, the composites exhibit higher values compared to $CoSb_3$ in the whole temperature range investigated. The values are particularly high in the x = 12 wt% sample (up to 70 mΩ.cm^{-1} at 300 K). The $\rho(T)$ data show a semiconducting behavior above 450 K. The presence of minority carriers is likely at the origin of this dependence since both types of carriers inevitably contribute to the electrical conduction. In $CoSb_3$, the $\rho(T)$ curves drop in a steeper way near 500 K compared to the composites. Beyond 700 K, it can be noticed that the data do not merge into a single curve owing to different relative densities d as shown by the following relation [36]

$$\sigma_{100\%} = \frac{2\sigma}{3d-1} \tag{7}$$

where σ is the electrical conductivity.

The temperature dependence of the total thermal conductivity of the ZnO/$CoSb_3$ composites is shown in Figure 13a. The combination of interfaces, wide defects and porosity contributes to decrease the values of κ in the composites compared to $CoSb_3$. The overall temperature dependence of the thermal conductivity is not influenced by the addition of ZnO nanoparticles. $\kappa(T)$ first decreases with temperature, shows a minimum near 650 K and then increases very slightly to reach a value of about 5.0 and 2.4 W.m^{-1}.K^{-1} at 800 K, for $CoSb_3$ and 12 wt% ZnO/$CoSb_3$, respectively. This behaviour is in agreement with the results of the literature for $CoSb_3$ [37].

Assuming that the Umklapp mechanism is the main phonon scattering mechanism in this temperature range, the lattice thermal conductivity is then expected to vary following a $1/T$ law. This contribution dominates the thermal transport between 300 and 600-650 K, as can be seen in Figure 13b. The enhancement of κ beyond 650 K may be due to an additional contribution to the electronic thermal conduction that can be attributed to the presence of the minority carriers resulting in electron-hole pairs (ambipolar contribution). Actually, in presence of electrons and holes, the electronic thermal conductivity can be expressed as [1]

$$\kappa = \kappa_{el} + \kappa_h + \kappa_{el-h} \quad (7)$$

where κ_{el} and κ_h are the contributions due to electrons and holes, respectively, and κ_{el-h} is the component due to the electron-hole pairs (ambipolar contribution). The Wiedemann-Franz law can be applied for the determination of κ_{el} and κ_h by considering the partial electrical conductivities. The ambipolar component, however, depends on the partial electrical conductivities of the electrons and holes as well as on the partial thermoelectric powers. The determination of these parameters requires applying a two-band model. Here, we therefore did not separate the bipolar from the lattice contribution. In the composites, for which the electrical resistivity is higher than for $CoSb_3$, the total thermal conductivity is still dominated by the lattice contribution.

The temperature dependence of the dimensionless thermoelectric figure of merit, *ZT*, calculated on the basis of the thermal and electrical measurements, is reported in Figure 14 for $CoSb_3$ and the ZnO/$CoSb_3$ composites. Except for the x = 12 wt% sample for which the high electrical resistivity is detrimental, the presence of ZnO slightly improves the thermoelectric performance of $CoSb_3$, with a maximum of 0.14 reached at 595 K for the x = 2 wt% sample due to the reduction of the thermal conductivity.

4. Conclusion

ZnO nanoparticles were introduced via a new route into the $CoSb_3$ skutterudite matrix to form composite materials and the effect of the presence of these oxide nanoparticles on the thermoelectric properties of the composites were investigated. ZnO agglomerates into irregular micron sized clusters located at the grain boundaries of the matrix. Both holes and phonons are affected by the large oxide defects and the porosity that increase with increasing the ZnO content. Low weight percentage of ZnO (2 wt %) enhances the dimensionless figure of merit with an improvement of up to 36% at 300 K decreasing unfortunately to 6% (within the uncertainty range of measurements) at 595 K, temperature of use of skutterudites. Further optimization might be achieved through improving the synthesis method to obtain a better dispersion of the ZnO nanoparticles and/or by introducing nanoparticles with a smaller size. Another worthwhile study would be to determine whether the enhancement of the *ZT* values survives the introduction of a filler atom in the cages of the crystalline structure. Such an attempt was successfully performed with Ag nanoparticles dispersed Ba-filled skutterrudites [38].

ACKNOWLEDGMENTS

Authors acknowledge the support by the European Network of Excellence CMA (Complex Metallic Alloys).

[1] D.M. Rowe, Thermoelectrics Handbook: Macro to Nano, CRC Taylor & Francis Group, Boca Raton, 2005.

[2] B. Lenoir, T. Caillat, H. Scherrer, in: T. Tritt (Ed.), Semiconductors and Semimetals, Academic Press, San Diego, 2001, Vol. 69, p. 101.

[3] A. Dauscher, B. Lenoir, H. Scherrer, T. Caillat, in: G. Pandalai (Ed.), Recent Research Developments in Materials Science, Research Signpost, 2002, Vol. 3, p. 181.

[4] C. Uher, in T. Tritt (Ed.), Semiconductors and Semimetals, Academic Press, San Diego, 2001, Vol. 69, p. 139.

[5] D. T. Morelli, G. P. Meisner, J. Appl. Phys. 77 (1995) 3777.

[6] G. A. Slack, in D. M. Rowe (Ed.), CRC Handbook of Thermoelectrics, CRC Taylor & Francis Group, Boca Raton, 2005, p. 407.

[7] D. J. Braun, W. Jeitschko, J. Less-Common Met. 72 (1980) 147.

[8] B. C. Sales, D. Mandrus, R. K. Williams, Science 272 (1996) 1325.

[9] L. D. Chen, T. Kawahara, X. F. Tang, T. Goto, T. Hirai, J. S. Dyck, W. Chen, C. Uher, J. Appl. Phys. 90 (2001) 1864.

[10] G. S. Nolas, M. Kaeser, R. T. I. Littleton, T. M. Tritt, Appl. Phys. Lett. 77 (2000) 1855.

[11] M. Puyet, A. Dauscher, B. Lenoir, C. Bellouard, C. Stiewe, E. Müller, J. Hejtmanek, J. Tobola Phys. Rev. B 75 (2007) 255110.

[12] L. D. Hicks, M. S. Dresselhaus, Phys. Rev. B 47 (1993) 12727.

[13] M. Toprak, C. Stiewe, D. Platzek, S. Williams, L. Bertini, E. Müller, C. Gatti, Y. Zhang, D. M. Rowe, Adv. Funct. Mater 14 (2004) 1189.

[14] X. Shi, L. Chen, J. Yang, G. P. Meisner, App. Phys. Lett. 84 (2004) 2301.

[15] Z. He, C. Stiewe, D. Platzek, G. Karpinski, E. Müller, S. Li, M. Toprak, M. Muhammed, J. Appl. Phys. 101 (2007) 043707.

[16] E. Alleno, L. Chen, C. Chubilleau, B. Lenoir, O. Rouleau, M. F. Trichet, B. Villeroy, J. Elect. Mater. 39 (2009) 1966.

[17] H. Li, X. Tang, Q. Zhang, C. Uher, Appl. Phys Lett. 94 (2009) 102114.

[18] X. Su, H. Li, G. Wang, H. Chi, X. Zhou, X. Tang, Q. Zhang, C. Uher, Chem. Mater. 23 (2011) 2948.

[19] M. Puyet, B. Lenoir, A. Dauscher, P. Weisbecker, S. J. Clarke, J. Solid. State Chem. 177 (2004) 2138.

[20] C. Chubilleau, B. Lenoir, A. Dauscher, C. Godart, Intermetallics 22 (2012) 47.

[21] J. Rodriguez-Carvajal, Phys. B 192 (1993) 55.

[22] C. Chubilleau, B. Lenoir, P. Masschelein, A. Dauscher, C. Godart, J. Elec. Mater. 41 (2012) 1181.

[23] X. Y. Zhao, X. Shi, L. D. Chen, W. Q. Zhang, S. Q. Bai, Y. Z. Pei, X. Y. Li, T. Goto, Appl. Phys. Lett. 89 (2006) 092121.

[24] X. Shi, L. D. Chen, S. Q. Bai, X. Y. Huang, X. Y. Zhao, Q. Yao, C. Uher, J. Appl. Phys. 102 (2007) 103709.

[25] N. Gothard, J. E. Spowart, T.M. Tritt, Phys. Stat. Solidi (A) Applications and Materials 207 (2010) 157.

[26] F. Porter, Zinc Handbook: Properties, Processing, and Use in Design, Marcel Dekker, Inc, New York, 1991.

[27] A. Janotti, C. G. Van de Walle, Rep. Prog. Phys. 72 (2009) 126501.

[28] M. Puyet, B. Lenoir, A. Dauscher, P. Pécheur, C. Bellouard, J. Tobola, J. Hejtmanek, Phys. Rev. B 73 (2006) 035126.

[29] E. Arushanov, K. Fess, W. Kaefer, Ch. Kloc, E. Bucher, Phys. Rev. B 56 (1997) 1911.

[30] J. Y. W. Seto, J. Appl. Phys. 46 (1975). 5247

[31] J. W. Orton, M. J. Powell, Rep. Prog. Phys. 43 (1980) 1263.

[32] C. H. Seager, J. Appl. Phys. 52 (1981) 3960.

[33] P. Ghosez, M. Veithen, J. Phys. C: Condens. Matter 19 (2007) 096002.

[34] T. Caillat, A. Borshchevsky, J.-P. Fleurial, J. Appl. Phys. 80 (1996) 4442.

[35] G. Kiriakidis, M. Suchea, S. Christoulakis, N. Katsarakis, Reviews on Advanced Materials Science 10 (2005) 215.

[36] R. Landauer, in: J.C. Garland, D. B. Tanner (Eds), Electrical Transport and Optical Properties of Inhomogeneous Media, American Institute of Physics New York, 1978, p. 2.

[37] J. W. Sharp, E. C. Jones, R. K Williams, P. M. Martin, B. C. Sales, B. J. Appl. Phys. 78 (1995) 1013.

[38] X. Zhou, G. Wang, L. Zhang, H. Chi, X. Su, J. Sakamoto, C. Uher, J. Mater. Chem. 22 (2012) 2958.

Table captions

Table I: Theoretical density $d_{composite}$, relative density d and lattice parameters a of $CoSb_3$ + x wt% ZnO.

x	$d_{composite}$ (g.cm^{-3})	d (%)	a (nm)
0	7.64	98	9.0350
2	7.59	91	9.0353
4	7.54	91	9.0342
8	7.43	89	9.0341
12	7.33	83	9.0357

Table II: Hole concentration p, Hall mobility μ_H, energy barrier E_B, density of trapping states N_t, width of the energy barrier b and calculated grain size L of $CoSb_3$ + x wt% ZnO. The Hall concentrations and mobilities were measured at 300 K. The four other parameters were inferred using Eq. (3), (4) and (5).

x	p (10^{18} cm^{-3})	μ_H ($cm^2.V^{-1}.s^{-1}$)	E_B (meV)	N_t (10^{12} cm^{-2})	b (nm)	L (μm)
0	2.48	2.48	15	15	5.4	2.2
2	1.43	1.43	21	21	8.4	3.1
4	1.16	1.16	31	31	11	3.7
8	1.22	1.22	32	32	11	3.9
12	0.83	0.83	40	40	15	1.3

Figure captions

Figure 1: X-ray diffraction patterns of the SPS densified $CoSb_3$ + *x* wt% ZnO samples.

Figure 2: Fracture image of the $CoSb_3$ + 2 wt% ZnO sample.

Figure 3: SEM (back-scattered electrons) images of the $CoSb_3$ + *x* wt% ZnO samples. The dark areas and the white zones represent ZnO and $CoSb_3$, respectively.

Figure 4: Temperature dependence of the thermopower *S* of the $CoSb_3$ + *x* wt% ZnO samples.

Figure 5: Temperature dependence of the hole concentration *p*.

Figure 6: Electrical resisitivity ρ as a function of temperature of the $CoSb_3$ + *x* wt% ZnO samples.

Figure 7: Hall mobility μ_H as a function of temperature.

Figure 8: (a) $\ln(\mu_H T^{1/2})$ vs $1/k_B T$ for the composite materials. (b) Best fit to the data following Eq.(3) to infer the barrier energy E_B.

Figure 9: Temperature dependence of the thermal conductivity κ of the $CoSb_3$ + *x* wt% ZnO samples.

Figure 10: Temperature dependence of the dimensionless figure of merit ZT of the $CoSb_3$ + x wt% ZnO samples.

Figure 11: Temperature dependence above room temperature of S for $CoSb_3$ and the four ZnO/$CoSb_3$ composites.

Figure 12: Temperature dependence at high temperatures of ρ of the $CoSb_3$ + x wt% ZnO samples.

Figure 13: κ as a function of temperature for $CoSb_3$ and the four ZnO/$CoSb_3$ composites: a) as a function of T, b) as a function of $1/T$ to highlight the dominant Umklapp processes between 300 and 600 K (the solid lines are guides for the eyes).

Figure 14: Temperature dependence of ZT of $CoSb_3$ + x wt% ZnO.

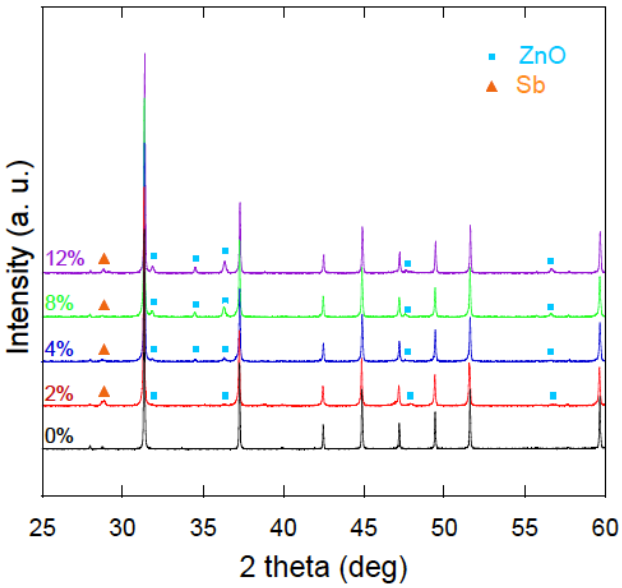

Figure 1

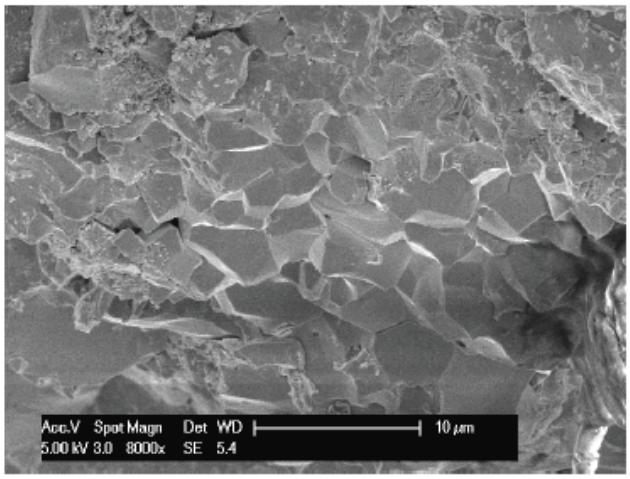

Figure 2

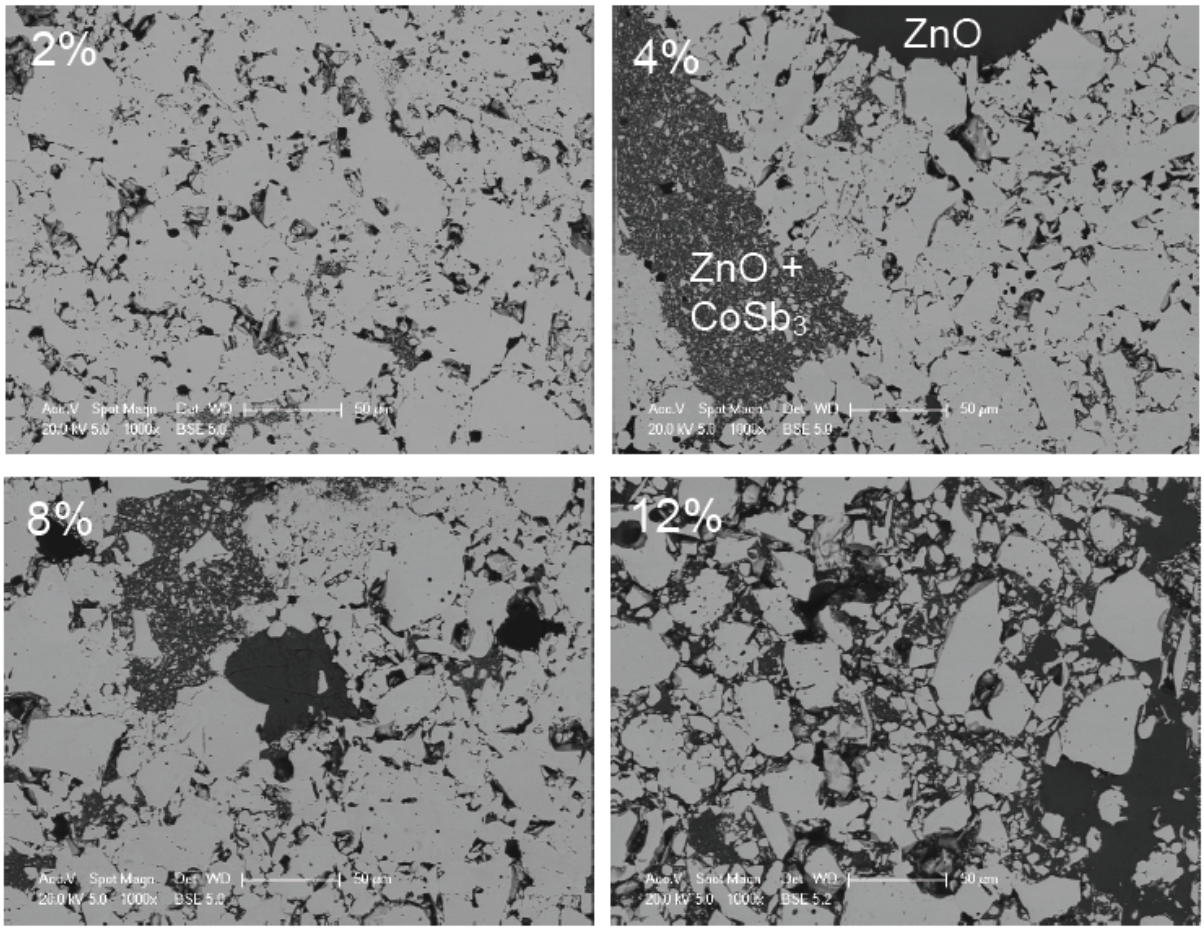

Figure 3

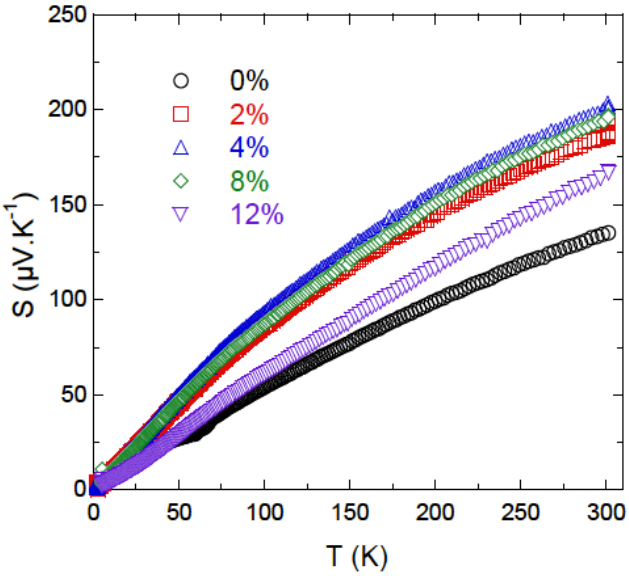

Figure 4

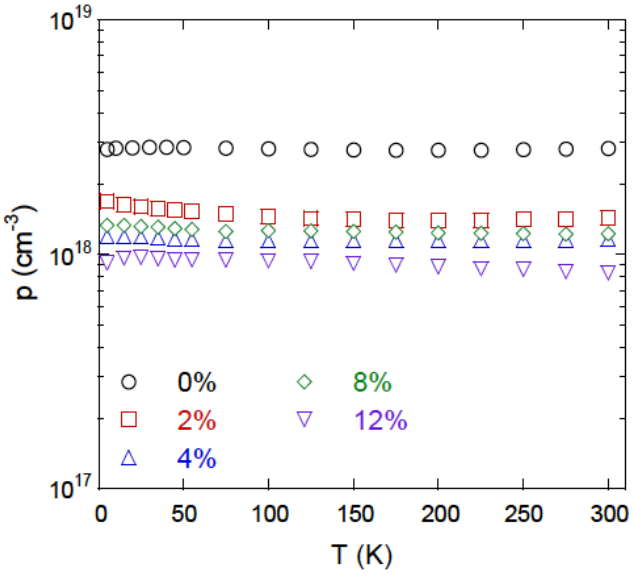

Figure 5

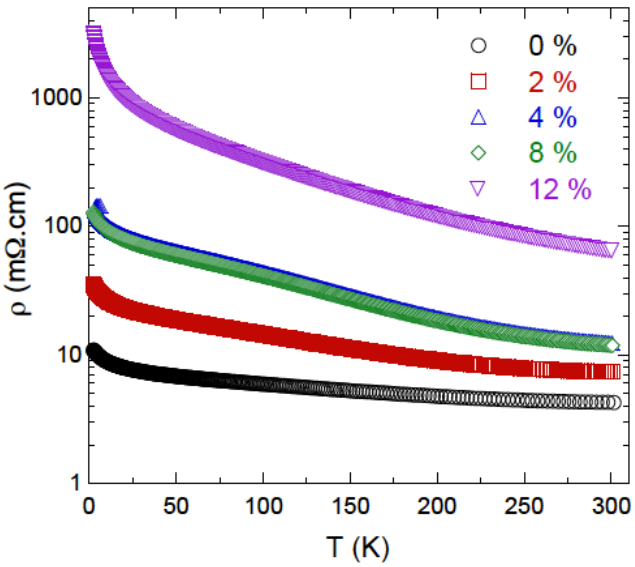

Figure 6

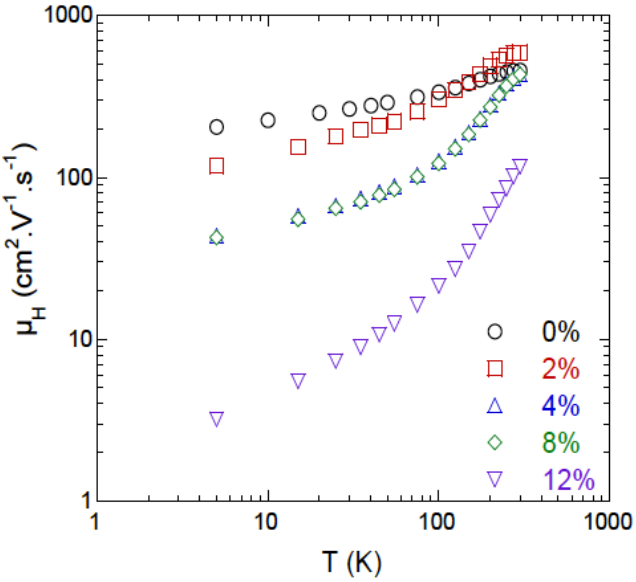

Figure 7

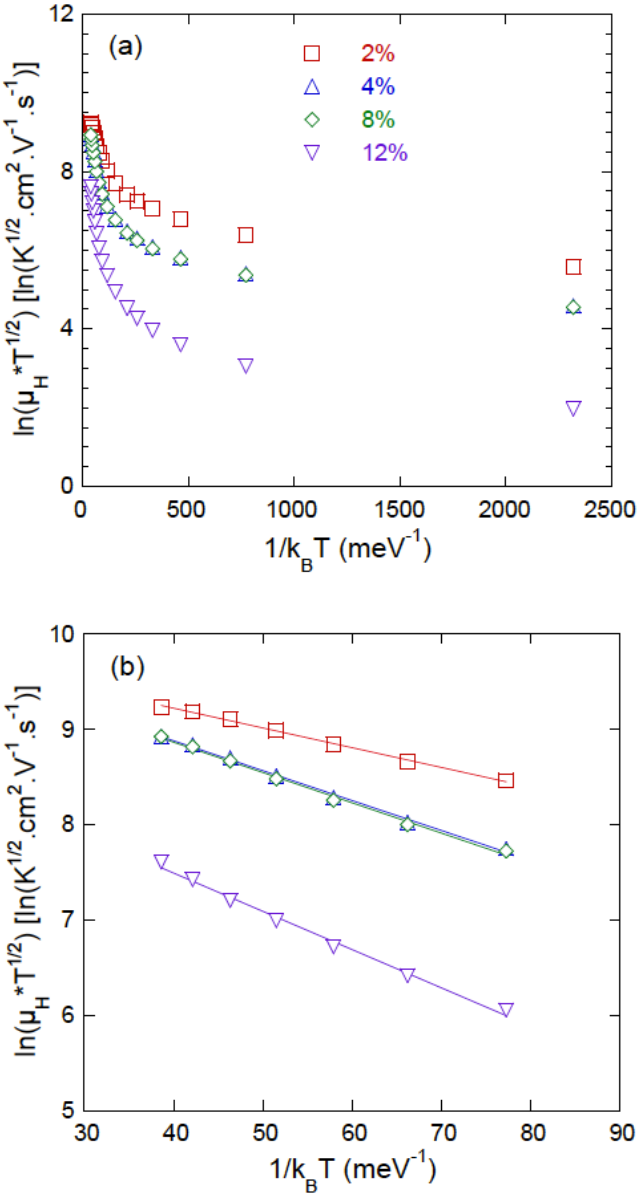
(a)
2%
4%
8%
12%
ln(μH*T1/2) [ln(K1/2.cm2.V-1.s-1)]
1/kBT (meV-1)
0
4
8
12
0
500
1000
1500
2000
2500
(b)
ln(μH*T1/2) [ln(K1/2.cm2.V-1.s-1)]
1/kBT (meV-1)
5
6
7
8
9
10
30
40
50
60
70
80
90

Figure 8

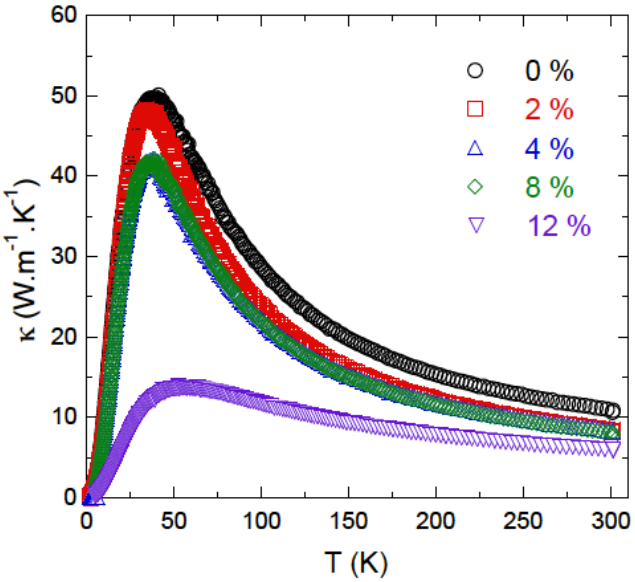

Figure 9

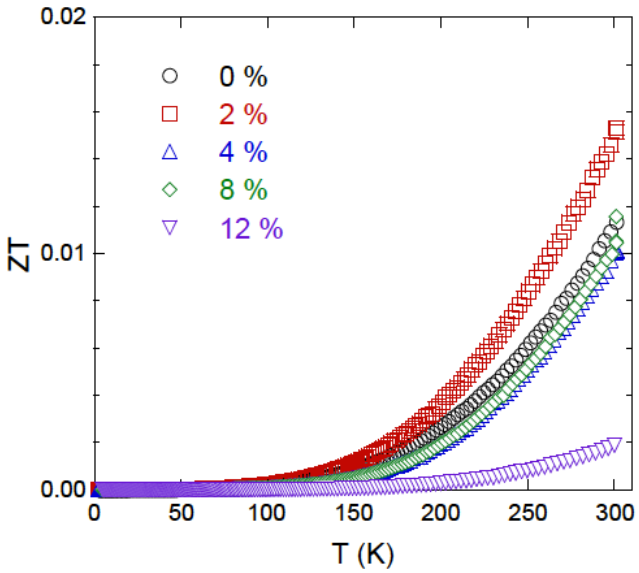

Figure 10

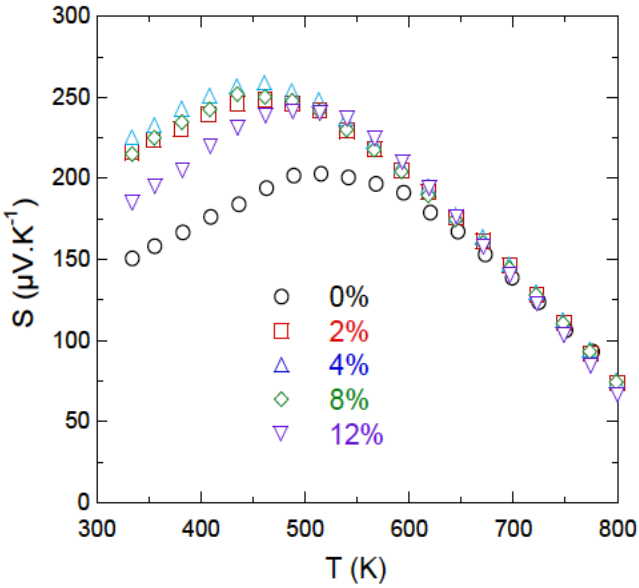

Figure 11

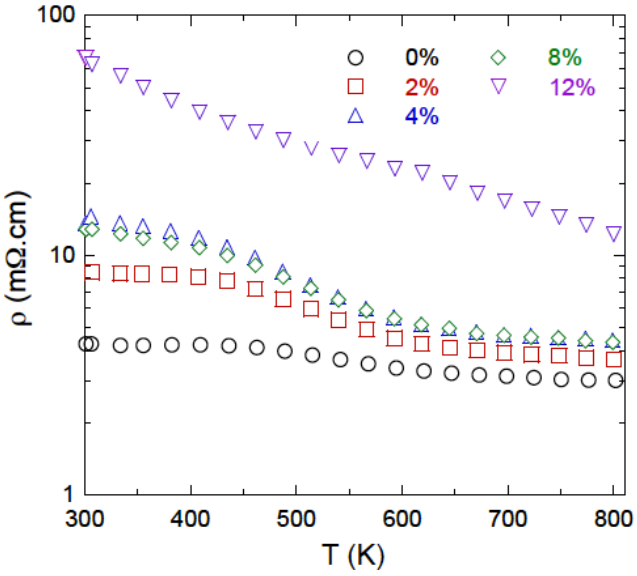

Figure 12

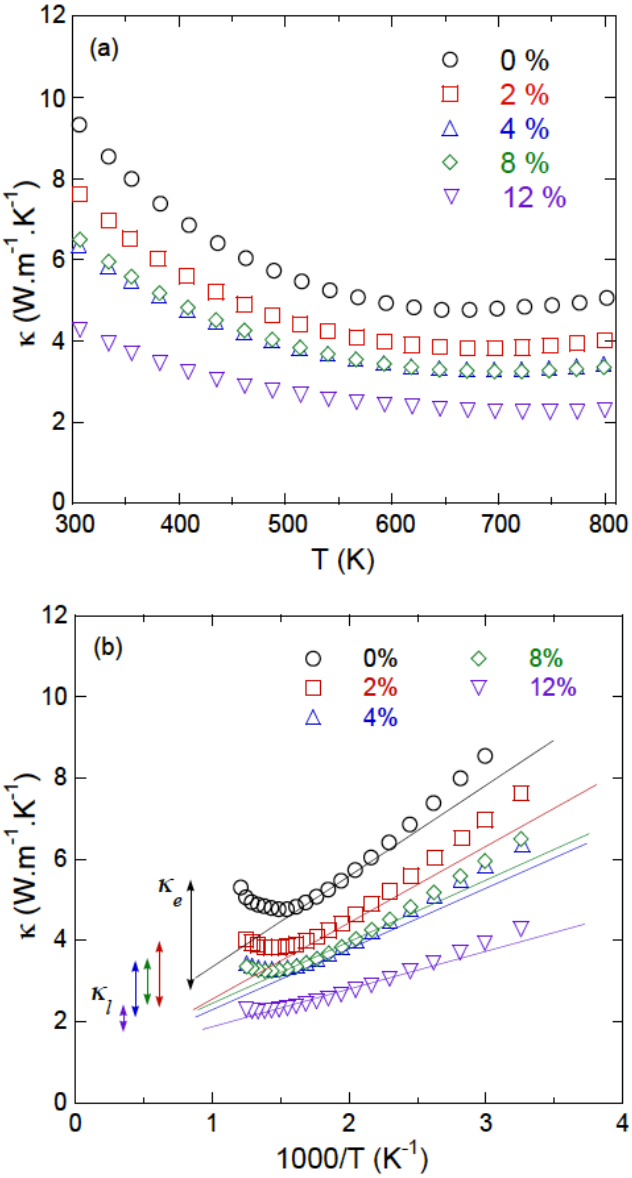

Figure 13

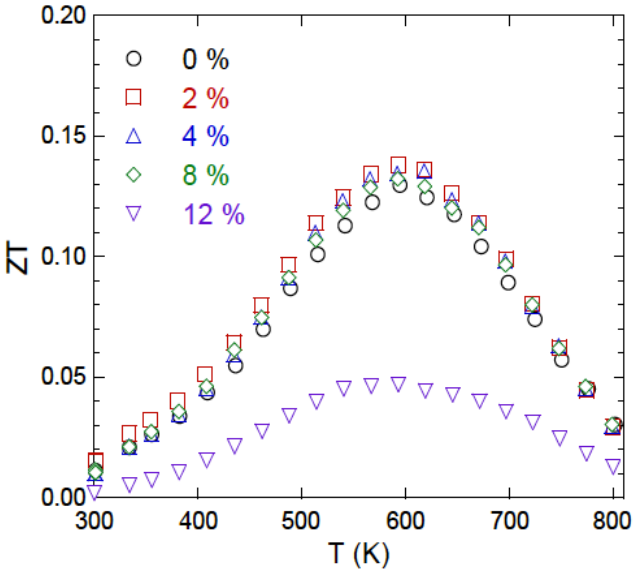

Figure 14